Structure and deformation correlation of closed cell aluminium foam subject to uniaxial compression

M. Saadatfar [a], M. Mukherjee [c], M. Madadi [a], G. E. Schröder-Turk [e], F. Garcia-Moreno [c,d], F. M. Schaller [e], S. Hutzler [b], A. P. Sheppard [a], J. Banhart [c,d], U. Ramamurty [f],

[a] *Research School of Physics and Engineering, The Australian National University, Canberra - 0200, Australia*

[b] *School of Physics, Trinity College Dublin, Ireland*

[c] *Helmholtz Centre Berlin, Hahn-Meitner-Platz 1, 14109 Berlin, Germany*

[d] *Technical University Berlin, Hardenbergstrasse 36, 10623 Berlin, Germany*

[e] *Institut für Theoretische Physik, Friedrich-Alexander Universität Erlangen-Nürnberg, Staudtstr. 7B, 91058 Erlangen, Germany*

[f] *Department of Materials Engineering, Indian Institute of Science, Bangalore 560012, India*

Abstract

We report the results of an experimental and numerical study conducted on a closed-cell aluminium foam that was subjected to uniaxial compression with lateral constraint. X-ray computed tomography (XCT) has been utilised to gain access into the 3D structure of the foam and some aspects of the deformation mechanisms. A series of advanced 3D image analyses are conducted on the 3D images aiming at characterising the strain localisation regions. We identify the morphological/geometrical features that are responsible for the collapse of the cells and strain localisation. A novel mathematical approach based on a Minkowski tensor analysis along with mean-intercept-length (MIL) technique were utilised to search for signatures of anisotropy across the foam sample and its evolution as a function of loading. Our results show that regions with higher degrees of anisotropy in the undeformed foam have a tendency to initiate the onset of cell collapse. Furthermore, we show that strain hardening occurs predominantly in regions with large cells and high anisotropy. We combine finite element method (FEM) with the tomographic images to simulate the mechanical response of the foam. We predict further deformation in regions where the foam is already deformed.

Key words: X-ray computed tomography; foams; compression test; finite element method.

1 Introduction

Metallic foams offer a combination of light weight, good thermal and acoustic insulation, as well as excellent mechanical response such as high structural efficiency under flexural loading conditions and outstanding capacity to absorb impact energy. These qualities make them ideal candidates for a variety of applications. The physical and mechanical properties of a foam depend directly on its cellular structure, which is highly stochastic in nature. Hence, there has been a great deal of effort in the recent past to understand the structure-property correlations in foams, so as to optimise the foam's mechanical performance for a given application.

Both elastic and plastic deformation in metallic foams are often inhomogeneous. The onset of plastic deformation under the influence of uniaxial compression is such that locally some cells begin to buckle and eventually collapse starting the onset of a highly localised collapse band [1–5]. An important question that is yet to be answered comprehensively in this context is the following: what are the structural and morphological factors that trigger the localised collapse of cells? The answer to this question will be sensitive to the imposed boundary condition. A thorough investigation of the geometrical and topological interconnectivity of the foam structure as well as its stress response to external loading will shed light into the complex dynamics of deformation associated with the foam. The aim of this study is to provide some key insights into this.

A large body of literature on research that has been conducted hitherto on the deformation mechanism of metallic foams is available. However, most of these studies are limited to the examination of cells and structural features that are present on the surface of the specimen [1, 2, 5, 6]. While these studies provide valuable insights into the understanding of compression/deformation mechanisms in cellular material, they do not truly reflect the inter-connectivity of the cells in the bulk as they do not have access to the spatial arrangement of cells in three-dimensions (3D). Moreover, these methods are invasive and usually involve cutting/polishing of the specimens therefore affecting the very structures/cells that they aim to study. Recently, X-ray computed microtomography (μ-CT) has been utilised to gain access into the 3D structure of the foams and also some of the deformation mechanisms. The main advantage of this technique is that it is non-destructive and allows for acquiring the full 3D structural information. In the present work, we employ μ-CT to analyse the deformation of a closed-cell aluminium foam sample subjected to uniax-

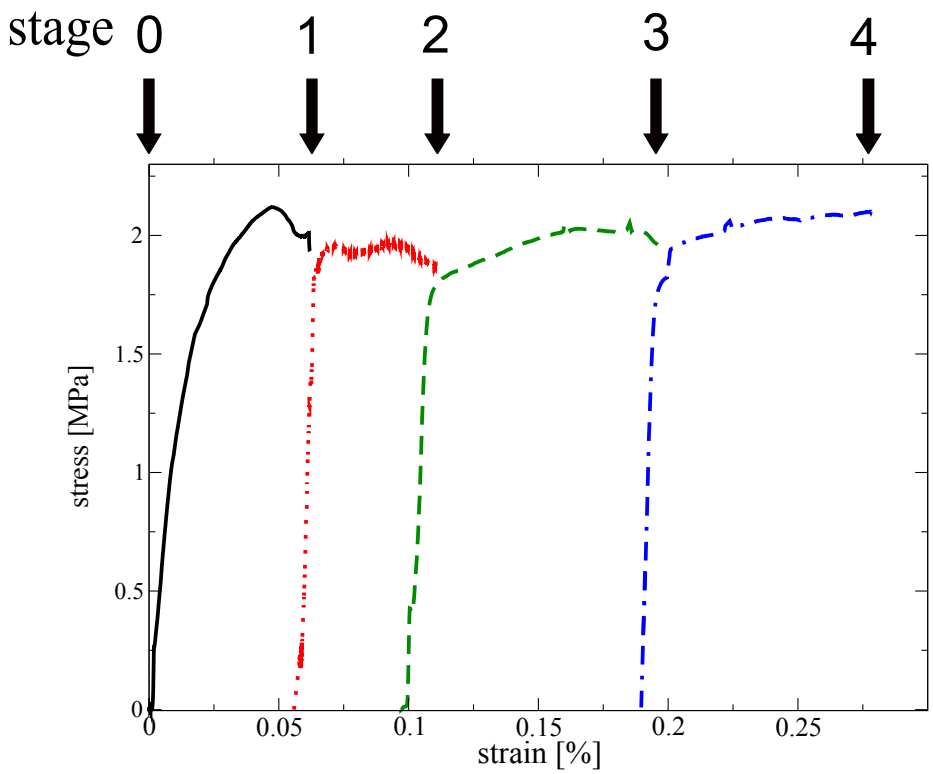

Figure 1. Experimental stress-strain response recorded during constrained compression of closed-cell Al foam, ALPORAS, specimen subjected to several stages of loading and unloading.

ial compression with lateral constraint, to successive stages of deformation (details in section 2) [7–9] . A series of advanced 3D image analyses, which allow for the measurement of cell size, shape and orientation in 3D directly from the images and aiming at characterising the strain localisation regions are conducted in order to identify the morphological/geometrical features that are responsible for the collapse of the cells and strain localisation. We combine the novel mathematical tool of Minkowski functionals and tensor analysis to extract anisotropy across the foam sample and observe its evolution as a function of loading. Additionally we carry out a mean-intercept-length (MIL) anisotropy analysis to validate the results of Minkowski tensor analysis. Then, we combine the tomographic data with the finite element method (FEM) to simulate the mechanical response of the foam. We also investigate the effect of strain hardening by calculating the elastic moduli of the sample at each stage of compression. This provides us an understanding of how the mechanical response of the foam sample changes before and after deformation localisation.

2 Compression experiment and tomographic reconstruction

A closed-cell ALPORAS aluminium foam supplied by Shinko Wire (Japan) was used in this study. ALPORAS has been used in many of the recent studies on mechanical testing of metallic foams as a standard material [3, 5, 10, 11], as it is supposed to have a homogeneous cellular structure [12]. Processing details and relevant properties of this foam are found in [12]. A sample of $50 \times 50\ mm^2$ section and 101 mm height was electro-discharge machined from a single large plate of ALPORAS foam. The thickness of the plate coincides with the loading direction. A die-steel sleeve of $50 \times 50\ mm^2$ inner cross section and 118 mm depth was used as lateral constraint during deformation. The inner area of the sleeve was chosen such that the sample fit easily into the sleeve. The foam sample was fixed into the sleeve with the help of screws (which enabled easy removal of the sample after deformation). After that a solid block of aluminium was placed on top of the foam sample. This entire setup was placed between parallel rigid plates of the universal testing machine and tests were performed [3]. The sample was compressed at a rate of $0.1\ mm/s$ (using a servo-hydraulic universal testing machine with displacement control). After imparting different amounts of strains (see Fig. 1) [3], the test sample was removed from the sleeve and imaged using μ-CT to acquire the 3D digital dataset (see Tab. 1). The strain applied to the foam is above elastic limits (see Fig. 1), so given the large cell sizes and the existence of imperfections and topological defects in the structure of the foam [3], the expectation is that the deformation is non-uniform [6, 13].

A microfocus X-ray source (100 kV acceleration voltage, 100 μA current and 5 μm spot size) and a flat panel detector (area $120 \times 120\ mm^2$, 2240×2368 pixel^2, pixel size 50 μm) both supplied by Hamamatsu (Japan), were used for imaging [15]. The foam was placed on a motor controlled rotating stage with the height of the foam perpendicular to the X-ray beam direction. The foam was rotated one degree at a time around its vertical axis and a radioscopic projection of the foam was taken after each rotation. A total of 360 projections with an exposition time of 8 s were obtained for a complete rotation of the foam. Tomographic cone beam reconstructions were then performed [16] on these 360 projections using the commercial software Octopus 8.1. With this setup, an effective voxel size (spatial resolution) of 45.58 μm is achieved. Fig. 2 shows the 3D reconstruction of our foam sample at different stages of compression. After acquiring images, deformation was continued by re-mounting the sample into the sleeve. Tomographic images of the same sample in more deformed states were acquired after further deformation.

The tomographic image consists of a cubic array of reconstructed linear X-ray attenuation values, each corresponding to a finite volume cube (voxel) of the sample. Binarised datasets (digital representation of foam structures) are

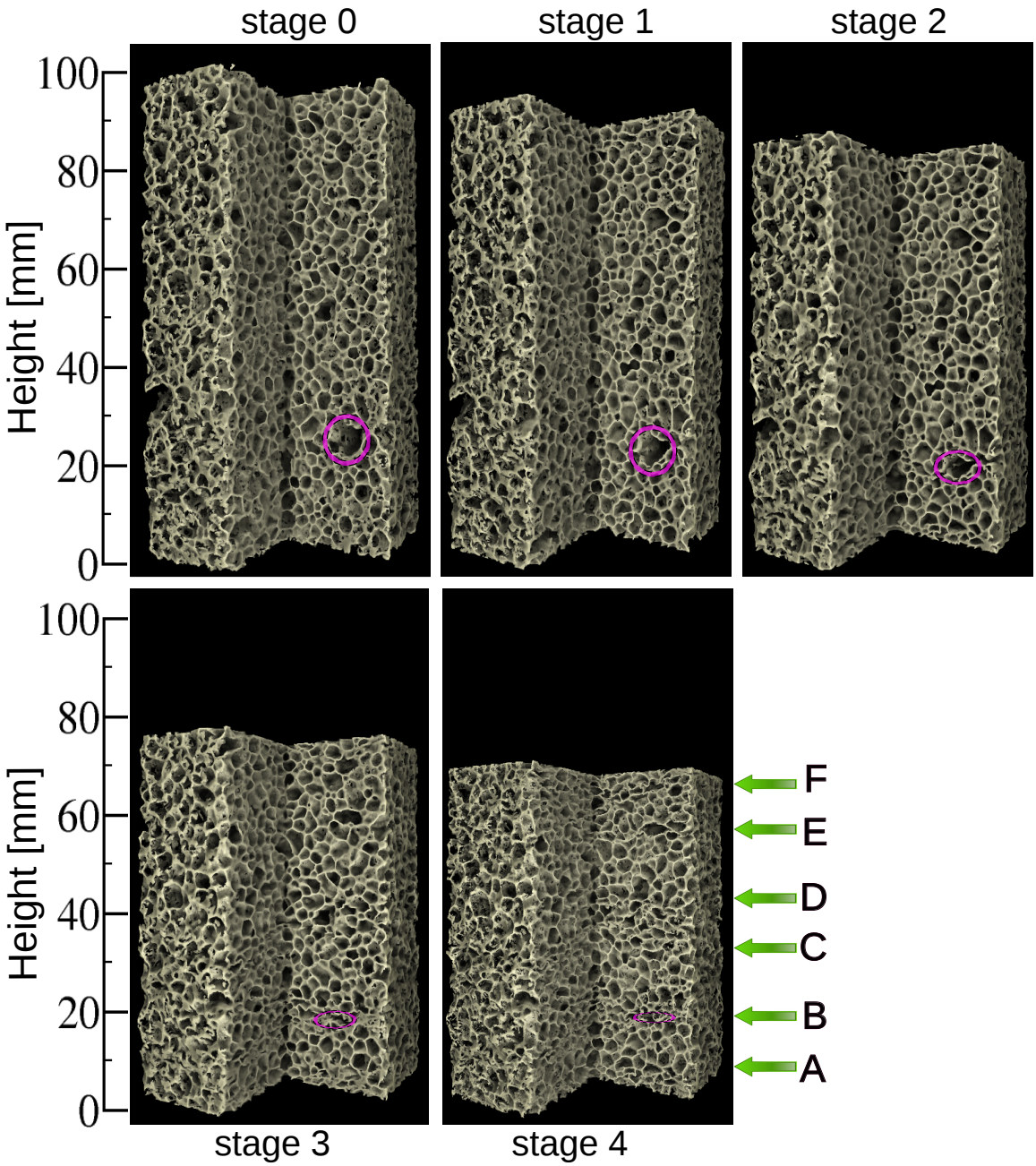

Figure 2. 3D reconstruction of the metallic foam sample examined in the present work at initial and four different stages of compression. These renderings are based on tomographic datasets of stages 0 through 4. Visualisation was performed with Drishti, an open source 3D volume rendering software [14]. The side bar A-F shows the regions where densification occurs (see Fig. 4).

used as the basis for all calculations presented in this paper. An example of the X-ray intensity histogram and a gray-scale X-ray density map for a 2D slice obtained from the uncompressed dataset, stage 0, is given in Fig. 3.

The intensity histogram ,Fig. 3(b), shows a distinct peak associated with

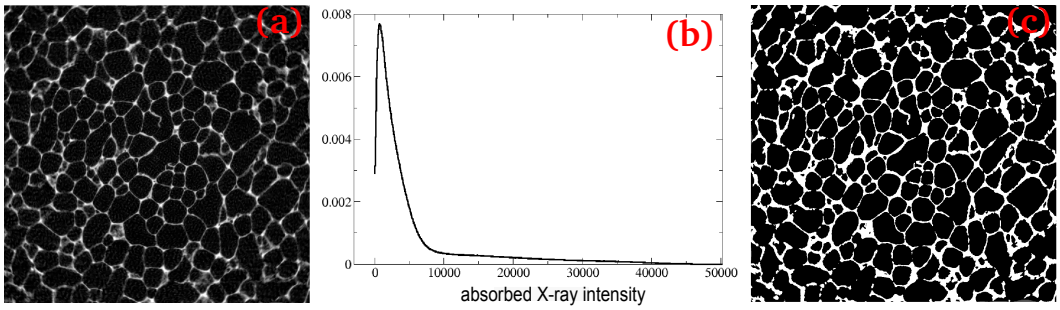

Figure 3. (a) Gray-scale X-ray density map of a slice of dataset 0 (tomogram of stage 0), (c) the same slice after binarisation, and (b) Normalised intensity histogram for the full image volume of dataset 0 (intensity values have arbitrary units and range between 0 and 65000). A cut-off value of 22500 of intensity is used to phase separate the image and to achieve target relative density, as obtained from weighing the precompressed sample (stage 0).

the pore phase (around 1080) but not a clear peak for the solid (metal) phase. This is usually due to very low solid fraction and also high value of noise-to-signal in the image. With the knowledge of the physical dimensions ($50.0 \times 50.0 \times 101.6\ mm$) and the weight of the specimen ($60.92\ g$), the density of our sample can be calculated as $0.24\ g/cm^3$. Knowing also the density of aluminium ($2.7\ g/cm^3$), the apparent (relative) density of our foam sample is $\rho_{al}/\rho_s \approx 0.089$ for the uncompressed stage. This knowledge enables us to choose the correct threshold value (22500) for binarisation of the tomograms so that the final segmented dataset has a solid fraction of the measured relative density of the sample. The resultant image based solid fraction (relative density) at the measured attenuation cut-off for dataset 0 is $\rho_{image} = 0.090$ (see Tab. 1). The segmentation process is followed by an isolated solid cluster removal to remove noise artefacts (small unconnected domains of solid in pores). However, the thickness of the solid wall in our compression samples is, in some places, only a few voxels. Therefore a three-step technique based on intensity gradients for image enhancement and segmentation is used to preserve the thin films [17]. Comparison of the grey-scale and binarised image of a 2D slice of stage 0 is shown in Fig. 3(a) and (c).

3 Morphological/geometrical analysis

3.1 Density

Relative density is extracted from the segmented datasets as the ratio of the sum of the total number of voxels belonging to the solid phase to the total number of voxels that make up the dataset (see Tab. 1). To better understand the spatial distribution of aluminium phase across each dataset at different

stages of compression, we calculate the density profile along the loading axis (Z axis). Fig. 4 shows the average density in each slice along Z calculated in sub-volumes of $50.0 \times 50.0 \times 5.5\ mm$. The choice of the sub-volume is made such that given the cells average diameters (see Tab. 1), the sub-volume contains at least one complete cell. Each sub-volume is then moved by one slice along the loading axis and the density is re-calculated again in the new sub-volume resulting in the generation of a data point in Fig. 4. This process is repeated until the moving sub-volume covers the whole length of each sample.

Fig. 4 suggests a relatively homogeneous density profile for dataset 0. However, as the sample is further compressed, the density (solid fraction per unit volume) increases steadily with the appearance of a prominent densification peak around the area with Z coordinates between $10 - 25\ mm$ and also at the two ends of the sample. The last stage of compression shows six distinct regions with higher densities, which are illustrated in Fig. 4. Note that the localised deformation bands B, C, D and E in stage 4 have widths of about

Compression stage	0	1	2	3	4
Accumulated strain [%]	0.00	4.93	9.56	17.64	25.32
Sample length [mm]	101.5	96.5	91.8	83.6	75.8
Measured density $\rho_{rel} = \rho/\rho_{al}$	0.089	0.094	0.098	0.108	0.112
Image density ρ_{image}	0.090	0.094	0.099	0.107	0.113
Average cell diameter $[mm]$	1.21±0.59	1.15±0.57	1.14±0.59	1.02±0.55	0.77±0.49
Average cell volume $[mm^3]$	16.2±3.1	14.7±2.8	13.2±2.2	11.5±2.9	9.3±2.7
Number of cells	7324	7377	7885	7982	8439
Average coord. no.	12.9±3.6	11.4±3.4	10.6±2.4	9.8±1.9	7.5±1.7

Table 1
Experimental (row 1-3) and image based (row 4-8) details of the compression progression derived from the tomographic images.

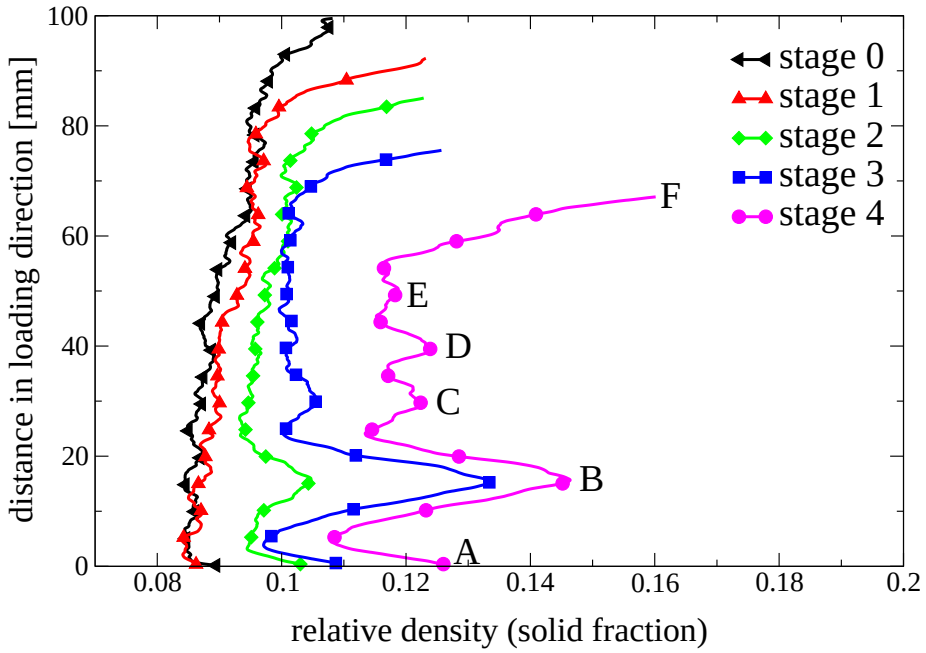

Figure 4. Density profile of the compression stages 0 to 4. Average density is calculated in a a sliding window of size 5.5 mm along the loading direction (Z direction). The sliding window moves slice by slice along the Z axis (simbols are sparsed for better viewing). Densification is pronounced in six regions in stage 4: A: bottom of the sample. B: around $Z \approx 10 - 25$ mm where most cells collapse. C: at around $Z \approx 30$ mm. D: at around $Z \approx 40$ mm. E: $Z \approx 50$ mm. F: top of the sample.

15, 10, 10 and 10 mm, respectively. This is in the order of 3 to 4 cell diameters. The distance between the deformation bands (peak-to-peak distance of the relative density) is about 3 cells. Both of these observations are consistent with previous studies of deformation mechanism in compressed ALPORAS foams [2, 6].

3.2 Cell identification

Any analysis of the volume, shape, orientation and coordination number of the cells requires the pore phase (cells) to be partitioned into separated cells. A watershed based pore partitioning algorithm [18,19] was applied to the 3D segmented datasets to separate individual cells. Fig. 5(a-b) shows 2D slices of the cell partitioned datasets of (stages 0 and 4). Here, the colour coding is merely for aiding the eye to distinguish neighbouring cells. The labelled datasets are now amenable to a range of geometrical analyses that are presented below.

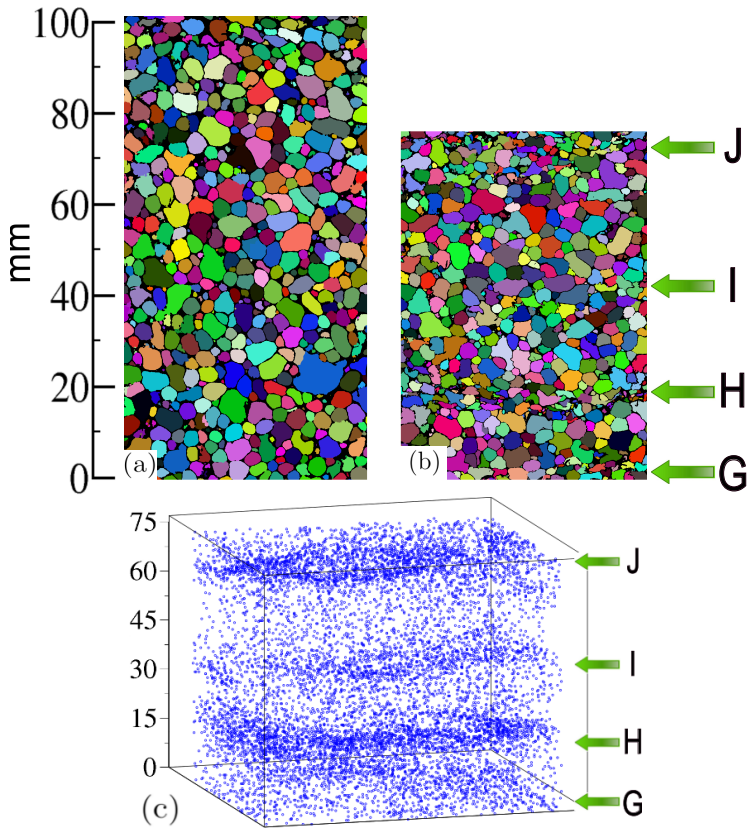

Figure 5. 2D slices ($x-z$ plane) selected from 3D datasets of the (a) undeformed stage and (b) deformed stage (stage 4) showing the collapsed cell bands labelled as G-J with a prominent collapsed band around H. This labelling is different from those shown in Figs. 2 and 4 where labels represented densification of solid phase. (c) Centre of mass of cells within stage 4 presented as a single point in 3D. The concentration of the centres of masses in parallel planes ($x-y$ planes) are evident.

3.3 Cell size/count

Fig. 6 shows a histogram of the cell sizes for each dataset. For the measurement of cell size, we use the equivalent diameter of a sphere whose volume is the same as a cell volume. In order to remove noise from the data, we filter out cells whose linear dimensions are smaller than $5 \times 5 \times 5$ volxels (volume$\approx$ 0.01 mm^3). All datasets exhibit a bimodal cell size distribution with an increasing shift towards higher population of smaller cells as the deformation progresses. Plastic buckling and collapse of cells is the reason for the observed shift in the size distribution. Counting the number of cells in each dataset confirms that an increase in loading increases the total number of cells in each dataset (see Tab. 1). While this increase in the number of cells could be attributed to the deformation and buckling of cell walls (they touch fully thus dividing one cell into two), this could also be an artifact from the

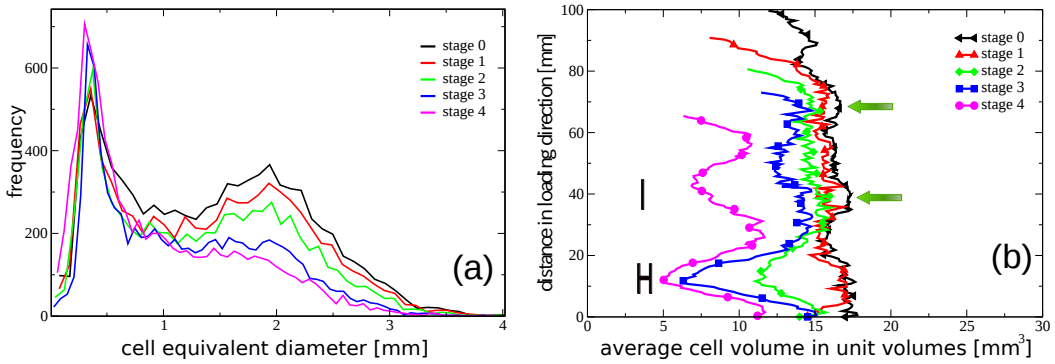

Figure 6. (a) Histogram of cell diameters. (b) Average cell volume along the loading axis for all datasets (simbols are sparsed to ease viweing the curves' trends). Progressing deformation of cells decreases their sizes around two main collapsed bands (H & I) in addition to the boundary cells at the top and bottom of the specimen (stage 4).

watershed algorithm [1]. To minimise this artifact, we visually inspect the result of cell partitioning to make sure that cell identification looks reasonable and correct input parameters are set [18]. These sets of parameters are used to label all 5 foam datasets.

We also calculate the spatial distribution of cells by measuring the average cell size in unit volumes across all the five datasets. Fig. 6(b) shows the measured average cell volume per unit volumes of $5.0 \times 5.0 \times 5.5$ mm in a sliding window whose height is 5.5 mm along the loading axis. Two peaks associated with smaller cell sizes appear in these datasets which are in the regions where most of the cells deform and collapse (shown as regions H and I). It is notable that in the uncompressed dataset (stage 0), there are two regions where cell volumes are larger than the average cell volumes in stage 0. These regions are indicated by arrows in Fig. 6(b). Both of these regions are where a collapse band of cells will develop at later stages of compression. Fig. 5(c) shows the centre of mass of cells in stage 4 as a single point in 3D. The collapse bands are clearly visible as regions with concentration of larger number of (smaller) cells. The cells collapse in almost parallel planes across the sample separated from one another by a distance of roughly $4-5$ cell diameters.

Compression stage	0	1	2	3	4
Average aspect ratio	0.47 ± 0.05	0.46 ± 0.05	0.45 ± 0.05	0.41 ± 0.06	0.37 ± 0.05
Average asp. ratio in regions where collapse occurs at stage 2,3,4	0.46 ± 0.06	0.46 ± 0.06	0.43 ± 0.07	0.35 ± 0.07	0.31 ± 0.07

Table 2
Average aspect ratio calculated as the ratio of $2R/L$. Systematic decrease in aspect ratio with increasing loading is notable.

3.4 Cell shape and orientation

Cell partitioning allows for more detailed analysis of individual cells. Most of shape/proportion analysis involves measuring the three linear dimensions of the cells. If it is assumed that the shape is a regular biaxial ellipsoid with long (L), intermediate (I) and small (S) axes, the aspect ratio is defined as the ratio of $2R/L$, where R is the equivalent radius of each cell. This definition leads to an aspect ratio of 1 for a perfect sphere. The aspect ratio calculations, summarised in Tab. 2, show that the average aspect ratio decreases as compression progresses. This observation implies that cells deviate further from a symmetric round shape upon deformation. We also calculated the average aspect ratio only in the main collapse band ($10 - 20\ mm$) and found it to be lower than its total average value across the whole dataset. For instance a value of 0.31 ± 0.07 compared with 0.37 ± 0.05 in dataset 4 (see Tab. 2 more details). This implies that, although some uniform deformation occurs as loading increases, deformation becomes increasingly more localised in some regions.

From the measurement of three primary cell axes one can also obtain information on cell orientation. We calculate the orientation of the primary axis L (longest axis) of each cell to describe the degree of preferential orientation of cells within each dataset. We calculate the *direction cosines* of the long axis of each cell ($cos(\alpha) = \frac{L \cdot \hat{x}}{\|L\|}, cos(\beta) = \frac{L \cdot \hat{y}}{\|L\|}, cos(\gamma) = \frac{L \cdot \hat{z}}{\|L\|}$) where α, β and γ are the angles between vector L and the three coordinate unit vectors ($\hat{x}$, $\hat{y}$ and

[1] As the cell walls begin to buckle, even if they will never touch, the deforming walls form a channel that changes in size as compression increases. Using the watershed algorithm, the size of these channels is the main criteria for determining if the cell should be digitally identified as two separate cells.

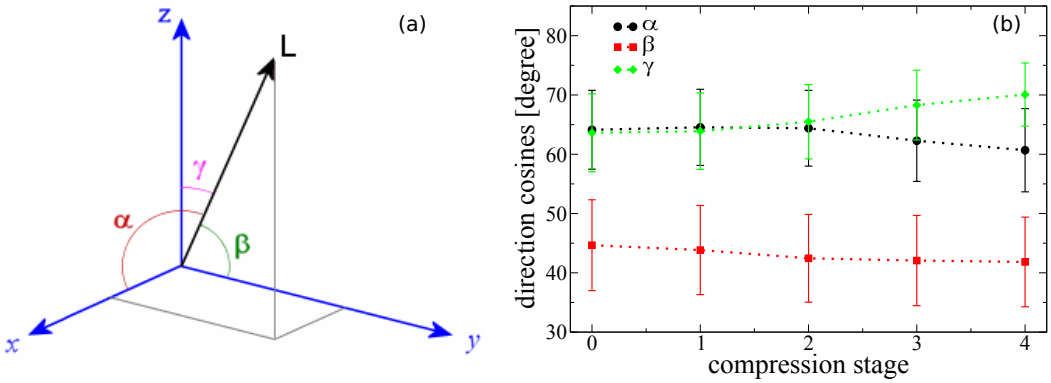

Figure 7. (a) Schematic representation of the orientation of long axis of the cells (L) represented by the direction cosines. (b) Evolution of the L with increasing compression. Each point is averaged over all the cells in each dataset.

$\hat{z}$) as demonstrated in Fig. 7(a).

Fig. 7(b) shows the average values of α, β and γ for stage 0-4. It is evident that the cells are oriented towards the y axis even in the uncompressed dataset. This could be the result of the manufacturing process of ALPORAS foam. In the making of ALPORAS, the release of gassing agents in molten aluminium creates bubbles that interact with their neighbouring bubble. These bubbles experience buoyancy due to gravity and as a result a foam growth direction is imposed. Additionally, when producing large blocks of ALPORAS, there is a small temperature gradient across the block which can also lead to inhomogeneous development of blowing agent and bubble generation. Before final cooling and solidification, the relatively aligned bubbles drain further and form cells which now have a preferred alignment [19–21].

Fig. 7(b) implies that as the compression progresses (more clearly in stages 2-4), γ increases whereas α and β decrease. This is expected as uniaxial loading is applied along the z direction. It is notable that the rate at which α decreases is larger than β suggesting that the cells tend to be elongated toward the x axis as they deform hence producing shear in x direction.

3.5 Coordination number

After cell identification and subsequent labelling of them, one can obtain a list of nearest neighbours of all the cells. From this list, it is straight-forward to determine the number of cells that are in contact with each cell either by sharing a wall or through the openings in the cell walls. This quantity is known as coordination number and we compute it for each cell and plot its distribution for each dataset as shown in Fig. 8(a). It is notable that the distribution changes towards lower values as the compression progresses. The

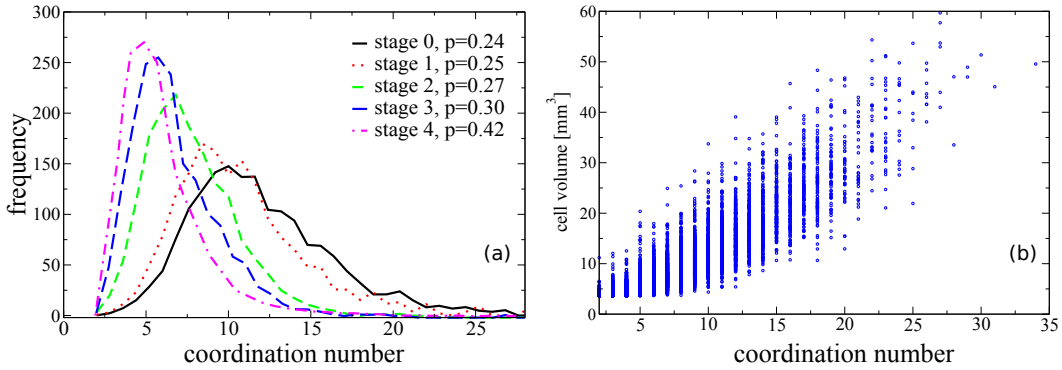

Figure 8. (a) Distribution of coordination number for all five datasets. (b) Correlation between volume of cells and their coordination number for dataset of stage 3.

average values of the coordination number are presented in Tab. 1. In section 3.3 we showed that cell sizes decrease as the applied load increases. This may suggest that smaller cells have lower coordination number on average. This can be tested by plotting the coordination number of each cell as a function of their volume. Fig. 8(b) shows such correlation for stage 3. This plot, although scattered, shows that smaller cells are surrounded by fewer number of cells, hence have lower coordination number [2].

For an ideal system of dry foam with monodispersed cell sizes, one would expect an average coordination number of ~ 13 [23]. It has been shown that the introduction of polydispersity to such foam systems decreases the average coordination number [21, 24]. Kraynik *et al.* in [25] use a measure of polydispersity, $p = < R^3 >^{2/3} / < R^2 > -1$, to demonstrate the influence of cell size distribution on the average coordination number in dry foams simulated by the Surface Evolver [26]. Here R is the equivalent radius of a sphere whose volume equals the volume of the cell. In our metallic foam compression datasets the calculated polydispersity values are p =0.24, 0.25, 0.27, 0.30 and 0.42 for stage 0, 1, 2, 3 and 4 respectively (see legend in Fig. 8(a)). The increase in polydisperisty with increasing loading is expected due to the division of cells as discussed in section 3.3. The average coordination numbers for stages 1-3 (see Tab. 1) are in very good agreement with Fig. 9 of [25] where an empirical relation between polydispersity and coordination number is presented.

3.6 Anisotropy

A signature of the deformation band can also be detected by measures of structural anisotropy which are defined *without* reference to a division of the

[2] In 2D cellular structures such an increase of cell area with coordination number is known as Lewis' Law [22]

foam into individual cells. Here we demonstrate that two different approaches for quantifying structural anisotropy, based on *Mean-Intercept Length (MIL)* tensor and *Minkowski* tensors respectively. We show that in the vicinity of the deformation band, the structure becomes significantly more anisotropic.

For a structure that allows for a clear subdivision into convex cells such as the foam studied here, the question of structural anisotropy and preferential alignment can be addressed by analysis of individual cells. In section 3.4 we discussed the aspect ratio of the cells and the angle between the cells' principal axis and the direction of strain. However, a method to quantify anisotropy and alignment without having to resort to an individual cell analysis is useful for several reasons. First, spatial structures exist for which the cell identification is ill-defined or ambiguous, e.g. sufficiently disordered open-cell foams or strut networks. Second, a cell-based measure is always strongly dependent on the cell identification algorithm (e.g. watershed algorithm, as used in this study). Given that anisotropy and alignment often are subtle effects, a direct measure that applies to the binarised dataset (without cell information) has advantages.

A commonly used anisotropy measure is the *MIL* analysis, largely developed for the analysis of bone and cellular structures [27–34]. For a biphasic structure consisting of a solid and a void phase, the **MIL** tensor quantifies anisotropy by counting the number of intersection points and the distance between them when randomly placed straight lines cross the solid-void (binarised dataset) interface for different fixed directions. In our measurements, we found that shooting $50,000$ lines throught the structure for any given angle produces reliable and reproducible results with error bar less than 0.005. The eigenvalues in each of the principal axes are then calculated for the 3D structure according to the distance between intercepts in the solid phase. The Degree of Anisotropy (DA) is calculated as the ratio of the minimum to maximum eigenvalues. In this notation, a DA value of 1 is reserved for isotropic structures whereas $DA{=}0$ represents aligned structures. Using this method we measure a DA of 0.618, 0.664, 0.705, 0.727 and 0.754 for datasets 0-4 respectively.

An alternative anisotropy measure is provided by the *Minkowski tensor* method, derived from an averaged distribution of interfacial directions [35]. Minkowski tensors [36, 37] are shape-measures that generalise the notion of volume, surface area and curvature to tensor-valued quantities, similar to the tensor of inertia and the surface tensor [38]. They have been successfully applied to free volume cells of liquid and jammed particle configurations [39, 40]. Because of their tensorial nature they offer, through ratios of their smallest-to-largest eigenvalues, a direct measure of shape anisotropy. Minkowski tensors are in principal integral quantities, i.e. representing averages over the whole dataset; however by using a sliding window the analysis can be performed locally, termed a *Minkowski tensor map* [36]. For a dataset representing a three-dimensional object, there are six different independent Minkowski ten-

sors in addition to the four scalar Minkowski functionals (volume, surface area, integrated mean curvature and Euler topology index) [37, 41]. Two of these, termed $W_1^{0,2}$ and $W_2^{0,2}$, are translation-invariant (i.e. independent of the choice of origin). Translation-invariance is important for structures where no physically motivated choice for the origin exists, such as structures with percolating components.

For a body K with bounding surface ∂K the two translation-invariant Minkowski tensors are defined as

$$W_1^{0,2}(K) := \frac{1}{3}\int_{\partial K} \hat{n} \otimes \hat{n}\ dA, \qquad W_2^{0,2}(K) := \frac{1}{3}\int_{\partial K} H\ \hat{n} \otimes \hat{n}\ dA \qquad (1)$$

The vector n is the surface normal vector of ∂K, $\otimes$ the tensor product of two vectors $(a \otimes b)_{ij} = a_i b_j$, and H is the point-wise (discrete) mean curvature of ∂K. For a metallic foam, the body K is the solid phase and ∂K is the solid-void interfacial surface. The tensor $W_1^{0,2}$ is readily interpreted as an integral measure that quantifies the fraction of surface area oriented in a given direction. With $\omega(n)$ the surface area of that fraction of ∂S with surface normal in direction of n, one obtains $\omega_1^{0,2}(K) = W_1^{0,2}(K) \int_{\mathcal{S}} \omega(n) dn$ with the unit sphere $\mathcal{S}$. Similarly, $W_2^{0,2}$ provides a measure for orientational distribution of curvatures.

Scalar anisotropy measures $\beta_1^{0,2}$ and $\beta_2^{0,2}$ are defined as the ratio of the minimal to the maximal eigenvalue of the Minkowski tensors $W_1^{0,2}$ and $W_2^{0,2}$. A value of 1 indicates an isotropic body, and deviations from 1 quantify the degree of anisotropy. Evaluated on the whole dataset, these provide immediate measures that specify how anisotropic the surface or curvature distribution of the body is as a whole. In order to provide a spatially resolved measure of anisotropy, a sliding window is used and $\beta_1^{0,2}$ and $\beta_2^{0,2}$ are computed for the part of ∂K within the sliding window and analysed as a function of the window position [36].

Fig. 9 shows DA and $\beta_2^{0,2}$ evaluated on sliding windows of 120^3 voxels ($\approx 5.5^3\ mm^3$), arranged on a grid, as a function of the position z of the sliding window centre in loading direction. Each data point represents an average over all window positions with the same value of z. The error bars represent the standard deviation of DA and $\beta_2^{0,2}$ within these subvolumes. The dominant compression zone between $10 - 20\ mm$, discussed above, is evidenced by a higher degree of anisotropy (lower values of DA and $\beta_2^{0,2}$ of the structure within this zone, as the strain is increased). This assessment of local structural anisotropy, obtained using two independent methods by analysing the binarised dataset without cell identification, agrees with cell-wise analyses using aspect ratio in Sec. 3.4.

An interesting but not very well-resolved feature that is detected in both of

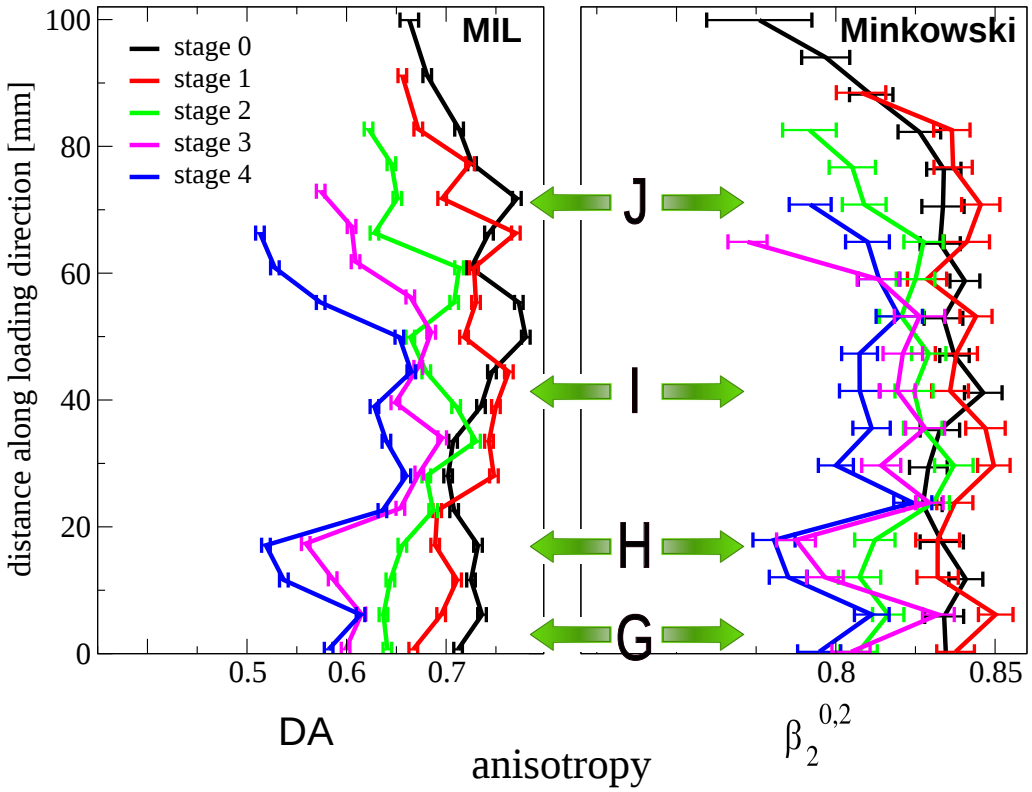

Figure 9. Anisotropy measures, *DA* (left) and $\beta_2^{0,2}$ (right), calculated based on *MIL* and *Minkowski tensors* repectivley and averaged over $5.5 \times 5.5 \times 5.5\ mm^3$ sub-volumes sliding along the loading axis. The data from both methods show a pronounced anisotropy around all four collapse bands in particular the main one ($10-20\ mm$). The result obtained in the undeformed dataset (stage 0) shows a relatively larger amount of anisotropy than other parts of the dataset just above the regions where bands of deformation will form (G-J). Both methods of anisotropy measures confirm this finding as shown in the figures above. The error bars ($\sigma/\sqrt{n}$) are standard deviation, σ over all n subvolumes in each layer. The similarities between this figure and Fig. 6(b) are notable even though Fig. 6(b) is calculated based on cell partitioning while this plot is derived from binarised datasets.

our anisotropy measures is the apparent slight increase of anisotropy in the uncompressed sample between $20-30\ mm$, see Fig. 9. This area is just above the region where most cells will collapse at later stages of compression. While more experimental data are needed to fully support this idea, it is tempting to suggest that the deformation is most favoured in this most *anisotropic* region of the sample, that will then move to the $10-20\ mm$ region of the final compressed sample. A similar behaviour is also observed above other deformation bands (G, I and J). This may suggest that anisotropy could be interpreted as a precursor to deformation.

Minkowski tensor analysis, in combination with a sliding window approach, offer a direct measure of anisotropy that may turn out physically relevant to

the compression of solid foams and that is directly and robustly computed on the binarised dataset. Importantly, a material which is anisotropic on one length scale may be isotropic on another length scale, which points towards the importance of the choice of the sliding window size, here fixed manually considering the typical cell size. The consistency of the results obtained by the MIL and the Minkowski tensor analysis is evidence that the conclusions of this section are independent of the method used to quantify anisotropy.

4 Finite element elastic simulations

Having successfully demonstrated the ability to describe the structure of the foam, we use the finite element method (FEM) to examine the elastic properties of the sample as a function of deformation. The FEM technique for simulating mechanical properties of microstructured materials has been extensively used in materials science, producing excellent agreement with experimental data of e.g., rock samples and cellular solids [8,42–46]. The FEM that we implemented uses a variational formulation of the linear elastic equations and finds the solution by minimising the elastic energy using a fast conjugate gradient method. Detailes of our FEM implementation can be found in the *Appendix*.

It is notable that althogh the metalic foam undergoes a plastic deformation during the compression process, however, at each stage of compression (marked as stages 0, 1, 2, 3 and 4) the foam starts to deform from zero strain and consequently exhibits elastic properties for a small range of initial strain, before plasitc deformaiton begins. This allows us to fully simulate the elastic response of the foam for each stage of compression using the implementation of FEM described in the *Appendix*.

The FEM simulation outputs the full tensorial stress response of our foam samples. Initial bulk and shear moduli of 76 GPa and 26 GPa (Young's modulus of 69 GPa) were assigned to the solid phase (aluminium) [12] and the simulations were performed on full datasets of each stage of compression. Fig. 10 shows the evolution of Young's modulus and shear components of the *compliance tensor* (see the *Appendix*) as compression progresses. A few points are noteworthy of pointing out; *i*) the Young's modulus in all directions for the uncompressed stage -stage 0- has a higher value than for stage 1. This can be understood by examining the stress-strain response in the first stage shown in Fig. 1. Clearly, the yield limit stress is reached at stage 1, after a small stress overshoot, marking the beginning of plastic deformation. The simulation values for Young's modulus for stage 0 correspond to pre-yielding, whereas the simulation values for stage 1 correspond to deformation immediately after the yield point. Therefore, it is expected that the microstructure shows a larger

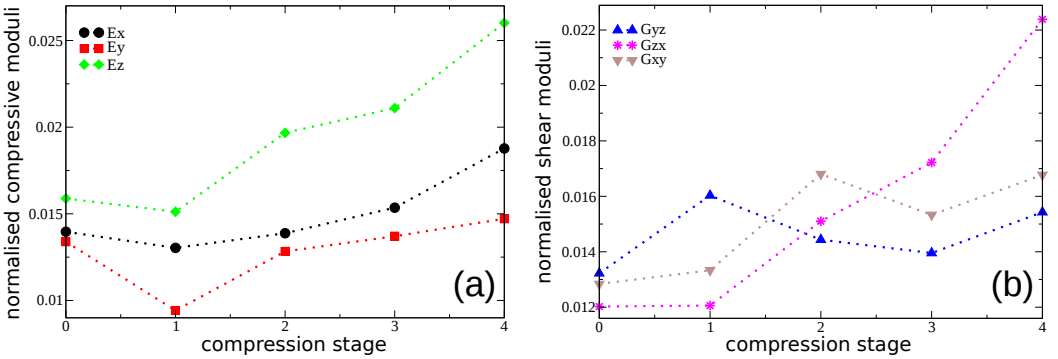

Figure 10. (a) Young's modulus of the foam sample (vertical axis) at each stage of compression derived from FEM simulations. The effective Young's moduli are normalised to that of solid phase (69 GPa). As the compression progresses, the compressive response of the foam becomes stronger. (b) Shear components of the compliance tensor as described in the text.

Young's modulus before the start of deformation in the sample. *ii*) From stage 1 to stage 4, values of Young's modulus increase as compression progresses, suggesting stiffening of the structure in all directions, in particular the loading direction (Y_z bsed on the notation used in the *Appendix*). *iii*) Fig. 10(b) also shows a strong increase of G_{zx} (shear component in the direction x in the $x-y$ plane) while the two other shear elements (shear in $y-z$ and $x-z$ planes) remain nearly invariant and behave similarly. This result is consistent with the cell orientation analysis presented in section 3.4 where we showed that loading causes the cells to deform such that their longest axis approaches the $x-y$ plane (increasing γ angle). Also, the decreasing rate of α is higher than of β which in turn causes shear in x direction.

Enhancement of G_{zx} is also expected from the uniaxial experimental setup with lateral confinement. Inspecting the reconstructed images from the tomogram (see Figs. 2 and 5) shows that the collapse of cells and density localisation occurs primarily in $x-y$ planes making the structure harder to shear in $x-y$ plane hence strengthening of G_{zx}.

We also repeat the FEM simulations in layers along the loading axis. In order to investigate the size effect in our simulations, two layer sizes of $50.0 \times 50.0 \times 5.5\ mm^3$ (approximately five cell diameter thick) and $50.0 \times 50.0 \times 13.5\ mm^3$ (approximately ten cell diameter thick) are considered and the Young's modulus is estimated for these. Fig. 11 shows the results of this analysis (5.5 mm height layer in the top row and 13.5 mm layer in the bottom row). Each point represents normalised Young's modulus on the vertical axis and the position z of the slab centre in loading direction. It is seen that all components of the Young's modulus increase as the compression increases. The continuous build up of Y_x and Y_y could be due to the lateral constrain while Y_z reflects the response of local structure to uniaxial loading with less influence to the con-

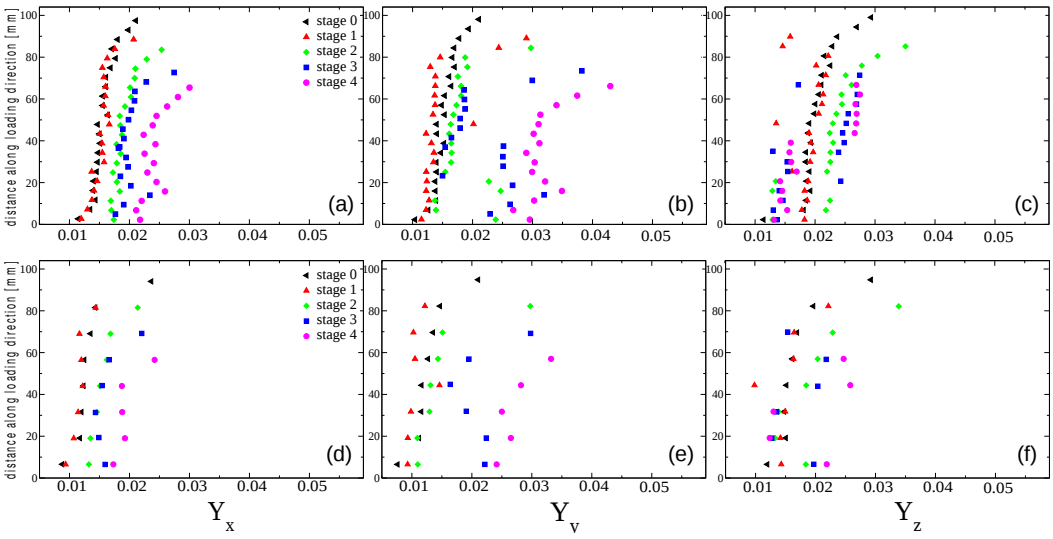

Figure 11. Effective Young's modulus of the foam sample (vertical axis) at each stage of compression along three principal axes Y_x, Y_y and Y_z derived from the FEM simulations. The effective Young moduli are normalized to that of the solid phase (69 GPa). As the compression progresses, the foam becomes stiffer. Top row represents data for slab size 5.5 mm bottom row for 13.5 mm.

fining boundary condition. Also the variability of Y_y seems to be higher than Y_x. This could be attributed to the orientation of cells as discussed in section 3.4. We are, however, unsure of an appropriate explanation for this variability.

The enhancement in Y_x and Y_y is quite pronounced around the region of the main collapse band ($10-20$ mm), whereas they decrease around this region as loading increases. A similar behaviour is also observed for the top part of the foam sample where a minor collapse is registered. This suggests that when a band starts to form, the Y_z in that part becomes weaker than in other parts of the sample and as a result the sample deforms easily upon further compression in this region. This trend is more visible in the 13.5 mm thick layer (Fig. 11(d-f)). Comparing the same component of Young's modulus in different layer sizes (Fig. 11(a-c)) shows that their overall trend is similar. This implies that the sub-volumes (layers) chosen for the simulations are representative and the simulation results are reliable for the chosen sizes.

Direct comparison of the experimental data (Fig. 1) with our FEM simulations (Fig. 10) is not possible. This is because of the lateral confinmet design of the steel sleve that is central to our compression experiment [3]. During the loading, the foam was not accessible from outside and therefore impossible to use an extensometer, neither contact nor non-contact extensometer. Hence an accurate experimental value for displacement associated exclusively with the foam sample was not measured by mounting a strain gage on the sample. Thus, the recorded displacement also includes that associated with the deformation of the load train.

Relative slope of successive compression stages	$\frac{1}{2}$	$\frac{2}{3}$	$\frac{3}{4}$
Experiment	0.72 ± 0.11	0.70 ± 0.17	0.71 ± 0.08
Simulation	0.77 ± 0.03	0.93 ± 0.03	0.81 ± 0.03

Table 3
Comparison of the experimental results and FEM simulations. We compare the relative changes in loading slopes from experimental stress-strain curves with the compressive moduli that was calculated using FEM simulations.

However, we can compare the relative changes in loading slopes (which is in fact proportional to the actual Y_z) with deformation for both simulations and experiment. From experimental stress-strain curve (see Fig. 1) we can measure the slopes of the linear part of the curves at the start of each stage, which are 0.097, 0.181, 0.259 and 0.366 for stage 1, stage 2, stage 3 and stage 4 respectively. Tab. 3 summarises the ratio of this slopes between successive stages as well as those obtained from simulation. The results show reasonable agreement between simulations and experiment within the errorbar.

5 Summary and conclusions

A block of ALPORAS foam was uniaxially compressed while laterally constrained. Tomograms were obtained in the undeformed and 4 deformed stages during interruptions of compression. Beside normal image analysis, a novel mathematical tool, Minkowski tensors, as well as MIL were used to measure the anisotropy in the datasets without the requirement of cell partitioning. FE modelling of elastic properties based on the tomographic data was carried out.

- As external loading increases, the cells begin to deform and their orientation changes such that the longest axis of the cells tends to lie in planes perpendicular to the loading direction.
- The uniaxial compression for the boundary condition of our experiment, causes the cells to deform and apparently divide into smaller sizes as opposing faces of the cells buckle and eventually touch. This results in an increase in the polydispersity of the sample with loading.
- The major part of deformation localises in layers that are mostly parallel and are apart from each other by $\approx 4 - 5$ cell diameter.
- Measurements of anisotropy based on two independent methods of Minkowski tensors and MIL applied show that regions with high degrees of local anisotropy in the undeformed foam are likely to induce collapse bands as loading increases. Additionally cell shape analysis show that local anisotropy of cells combined with cells orientation and size can also be a player in triggering

localised deformation.

- Finite element analysis of the entire sample correctly predicts a lower Young's modulus after passing yield limit stress at the end of stage 1. The FEM analysis of individual layers reveals that the effect of lateral constraint on Y_x and Y_y could be that of strain build up, while Y_z predicts further deformation of structure in regions where foam is already deformed.

The combination of experimental and numerical tools employed in this work shows the potential to predict physical properties from images of complex cellular materials. This could be further developed in the future towards a routinely applied method.

Acknowledgements

MS thanks ARC Discovery (DP0881458) for the financial support. MS also thanks Eva Franklin for proofreading the first draft and Ajay Limay for assisting with the creation of Figure 2. GEST acknowledges support by the German research foundation (DFG) through grant SCH R1148/3-1. SH, JB and FGM acknowledge funding from the European Space Agency (MAPs AO-99-108 and AO-99-075).

Appendix

The segmented datasets give a 3D representation of the foam's structure and each three-dimensional volume element in the segmented image is called a voxel (see sec. 2). In our FEM implementation, each voxel is taken to be a cubic finite element. In order to calculate the mechanical response of the foam samples, an applied displacement field is distributed initially across all the voxels such that a constant strain is imposed along the length of the sample [44]. For a given microstructure, subject to applied fields or other boundary conditions, the final elastic displacement distribution is such that the total energy (E) stored is minimised:

$$E = \frac{1}{2} \int_v \epsilon_{ij} \; C_{ijkl} \; \epsilon_{kl} \; dv \tag{2}$$

Here ϵ is the strain field (a 2^{nd} rank tensor), C is the stiffness tensor (a 4^{th} rank tensor), dv is the volume element and the integration is over the entire sample. Minimisation of elastic energy means that the gradient of the energy with respect to elastic displacement variables, u_m, is zero ($\frac{\partial E}{\partial u_m} = 0$). From

Eq.2, we can write: $C_{ijkl} = \frac{\partial^2 E}{\partial \epsilon_{ij} \partial \epsilon_{kl}}$. The relationship between stress and strain can be expressed as $[\sigma] = [C][\epsilon]$ where $[\sigma]$ and $[\epsilon]$ are stress and strain tensors respectively. In the most generalised form, $[C]$ has 81 independent elements. However, using the symmetry (*minor* and *major* symmetries) and also the fact that experimental set-up imposes orthotropic (transverse) symmetry on our foam sample [47], $[C]$ can be re-written using Voigt's notation which contains only nine independet elements:

$$C_{ijkl} = \begin{pmatrix} C_{11} & C_{12} & C_{13} & 0 & 0 & 0 \\ C_{21} & C_{22} & C_{23} & 0 & 0 & 0 \\ C_{31} & C_{32} & C_{33} & 0 & 0 & 0 \\ 0 & 0 & 0 & C_{44} & 0 & 0 \\ 0 & 0 & 0 & 0 & C_{55} & 0 \\ 0 & 0 & 0 & 0 & 0 & C_{66} \end{pmatrix} \tag{3}$$

Here $C_{12} = C_{21}$, $C_{13} = C_{31}$ and $C_{23} = C_{32}$. The inverse of this matrix is known as compliance tensor whose elements are directly proportional to the mechanical properties of the structure and is commonly written as [48]:

$$S_{ijkl} = \begin{pmatrix} \frac{1}{Y_x} & -\frac{\nu_{xy}}{Yx} & -\frac{\nu_{xz}}{Yx} & 0 & 0 & 0 \\ -\frac{\nu_{yx}}{Yy} & \frac{1}{Y_y} & -\frac{\nu_{yz}}{Yy} & 0 & 0 & 0 \\ -\frac{\nu_{zx}}{Yz} & -\frac{\nu_{zy}}{Yz} & \frac{1}{Y_z} & 0 & 0 & 0 \\ 0 & 0 & 0 & \frac{1}{G_{yz}} & 0 & 0 \\ 0 & 0 & 0 & 0 & \frac{1}{G_{yx}} & 0 \\ 0 & 0 & 0 & 0 & 0 & \frac{1}{G_{xy}} \end{pmatrix} \tag{4}$$

where Y_i is the Young's modulus along axis i, G_{ij} is the shear modulus in direction j on the plane whose normal is in direction i, and ν_{ij} is the Poisson's ratio that corresponds to a contraction in direction j when an extension is applied in direction i [3]. All the elements in tensor S can be calculated from our FEM simulations, which allows for a complete understanding of the full tensorial stress response of anisotropic materials such as our foam sample.

[3] Values of Poisson's ratio calculated in our simulations are very close to 0.

References

[1] H. Bart-Smith, A. Bastawros, D. Mumm, A. Evans, D. Sypeck, and H. Wadley *Acta materialia*, vol. 46, no. 10, pp. 3583–3592, 1998.

[2] A. Bastawros, H. Bart-Smith, and A. Evans *Journal of the Mechanics and Physics of Solids*, vol. 48, no. 2, pp. 301–322, 2000.

[3] M. Kolluri, S. Karthikeyan, and U. Ramamurty *Metallurgical and Materials Transactions A*, vol. 38, pp. 2006–2013, 2007.

[4] M. Kolluri, M. Mukherjee, F. Garcia-Moreno, J. Banhart, and U. Ramamurty *Acta Materialia*, vol. 56, no. 5, pp. 1114–1125, 2008.

[5] M. Mukherjee, M. Kolluri, F. Garcia-Moreno, J. Banhart, and U. Ramamurty *Scripta Materialia*, vol. 61, no. 7, pp. 752–755, 2009.

[6] Y. Mu, G. Yao, L. Liang, H. Luo, and G. Zu *Scripta Materialia*, vol. 63, no. 6, pp. 629 – 632, 2010.

[7] M. R. Fetterman, E. Tan, L. Ying, R. A. Stack, D. L. Marks, S. Feller, E. Cull, J. M. Sullivan, J. D. Munson, S. T. Thoroddsen, and D. J. Brady *Optics Express*, vol. 7, no. 5, pp. 186–197, 2000.

[8] M. Saadatfar, C. H. Arns, A. Sakellariou, T. J. Senden, A. P. Sheppard, R. M. Sok, W. Schrof, and M. A. Knackstedt *Physica A*, vol. 339, pp. 131–136, 2004.

[9] C. Kádár, E. Maire, A. Borbély, G. Peix, J. Lendvai, and Z. Rajkovits *Materials Science and Engineering A*, vol. 387, pp. 321–325, 2004.

[10] J. Grenestedt *Journal of the Mechanics and Physics of Solids*, vol. 46, no. 1, pp. 29–50, 1998.

[11] I. Jeon and T. Asahina *Acta Materialia*, vol. 53, no. 12, pp. 3415–3423, 2005.

[12] T. Miyoshi, M. Itoh, S. Akiyama, and A. Kitahara *Advanced Engineering Materials*, vol. 2, no. 4, pp. 179–183, 2000.

[13] M. Luxner, J. Stampfl, and H. Pettermann *International Journal of Solids and Structures*, vol. 44, no. 9, pp. 2990–3003, 2007.

[14] A. Limaye, "Available from: http://anusf.anu.edu.au/vizlab/drishti/,"

[15] F. Garcia-Moreno, M. Fromme, and J. Banhart *Advanced Engineering Materials*, vol. 6, no. 6, pp. 416–420, 2004.

[16] L. A. Feldkamp, L. C. Davis, and J. W. Kress *J. Opt. Soc. America A*, vol. 1, pp. 612–619, 1984.

[17] A. P. Sheppard, R. M. Sok, and H. Averdunk *Physica A*, vol. 339, pp. 145–151, 2004.

[18] M. Saadatfar, A. Sheppard, and M. A. Knackstedt, *Advances in X-ray Tomography for Geomaterials: Grain partitioning and its applications*, vol. ISBN 1-905209-60-6. Wiley Online Library, 2006.

[19] M. Saadatfar. PhD thesis, The Australian National University, 2006.

[20] Z. Song and S. Nutt *Metallurgical and Materials Transactions A*, vol. 39, no. 9, pp. 2215–2227, 2008.

[21] M. Saadatfar, F. Garcia-Moreno, S. Hutzler, A. Sheppard, M. Knackstedt, J. Banhart, and D. Weaire *Colloids and Surfaces A: Physicochemical and Engineering Aspects*, vol. 344, no. 1-3, pp. 107–112, 2009.

[22] D. Weaire and N. Rivier *Contemporary Physics*, vol. 25, no. 1, pp. 59–99, 1984.

[23] A. M. Kraynik, D. A. Reinelt, and F. van Swol *Phys. Rev. E*, vol. 67, p. 031403, 2003.

[24] A. M. Kraynik, D. A. Reinelt, and F. van Swol *Phys. Rev. Lett.*, vol. 93, p. 208301, Nov 2004.

[25] A. Kraynik *Advanced Engineering Materials*, vol. 8, no. 9, 2006.

[26] K. A. Brakke *Experimental Mathematics*, vol. 1, no. 2, pp. 141–165, 1992.

[27] W. J. Whitehouse *J. Microsc.*, vol. 101, no. 2, pp. 153–168, 1974.

[28] T. Harrigan and R. Mann *J. Mater. Sci.*, vol. 19, pp. 761–767, 1984.

[29] A. Odgaard *Bone*, vol. 20, no. 4, pp. 315 – 328, 1997.

[30] M. Wald, B. Vasilic, P. Saha, and F. Wehrli *Med. Phys.*, vol. 34, no. 3, pp. 1110–1120, 2007.

[31] L. Mathieu, T. Mueller, P. Bourban, D. Pioletti, R. Muller, and J. Manson *Biomaterials*, vol. 27, no. 6, pp. 905–916, 2006.

[32] M. Chiang, X. Wang, F. Landis, J. Dunkers, and C. Snyder *Tissue Eng.*, vol. 12, no. 6, pp. 1597–1606, 2006.

[33] D. Inglis and S. Pietruszczak *Int. J. Solids Struct.*, vol. 40, no. 5, pp. 1243–1264, 2003.

[34] R. Ketcham and T. Ryan *J. Microsc.*, vol. 213, no. 2, pp. 158–171, 2004.

[35] G. E. Schrder-Turk, W. Mickel, S. C. Kapfer, M. A. Klatt, F. M. Schaller, M. J. F. Hoffmann, N. Kleppmann, P. Armstrong, A. Inayat, D. Hug, M. Reichelsdorfer, W. Peukert, W. Schwieger, and K. Mecke *Advanced Materials*, vol. 23, no. 22-23, pp. 2535–2553, 2011.

[36] G. E. Schröder-Turk, S. C. Kapfer, B. Breidenbach, C. Beisbart, and K. Mecke *J. of Microscopy*, vol. 238, pp. 57–74, 2010.

[37] R. Schneider and W. Weil, *Stochastic and Integral Geometry (Probability and Its Applications)*. Springer, 2008.

[38] M. Doi and T. Ohta *The Journal of Chemical Physics*, vol. 95, p. 1242, 1991.

[39] G. E. Schröder-Turk, W. Mickel, M. Schröter, G. W. Delaney, M. Saadatfar, T. J. Senden, K. Mecke, and T. Aste *EPL (Europhysics Letters)*, vol. 90, p. 34001, 2010.

[40] S. C. Kapfer, W. Mickel, F. M. Schaller, M. Spanner, C. Goll, T. Nogawa, N. Ito, K. Mecke, and G. E. Schröder-Turk *J. Stat. Mech.: Theory and Exp.*, vol. 2010, no. 11, p. P11010, 2010.

[41] K. Mecke vol. 554 of *Lecture Notes in Physics*, pp. 111–184, Springer Verlag, 2000.

[42] M. Saadatfar, C. Arns, M. Knackstedt, and T. Senden *Colloids and Surfaces A: Physicochemical and Engineering Aspects*, vol. 263, no. 1-3, pp. 284–289, 2005.

[43] M. Knackstedt, C. Arns, M. Saadatfar, T. Senden, A. Sakellariou, A. Sheppard, R. Sok, W. Schrof, and H. Steininger *Advanced Engineering Materials*, vol. 7, no. 4, pp. 238–243, 2005.

[44] E. J. Garboczi and A. R. Day *Journal of Mathematical Physics*, vol. 43, no. 9, pp. 1349–1362, 1995.

[45] M. A. Knackstedt, C. H. Arns, M. Saadatfar, T. J. Senden, A. Limaye, A. Sakellariou, A. P. Sheppard, R. M. Sok, W. Schrof, and H. Steininger *Proc. Royal. Society*, vol. 462, pp. 2833–2862, September 2006.

[46] M. Madadi, A. Jones, C. Arns, and M. Knackstedt *Computing in Science & Engineering*, vol. 11, p. 65, 2009.

[47] W. Slaughter and B. Verlag *Current Science*, vol. 84, no. 2, p. 232, 2003.

[48] A. Boresi, R. Schmidt, and O. Sidebottom, *Advanced mechanics of materials, 1993*. John Wiley, New York, 1993.